Materials & Design 238 (2024) 112738

Contents lists available at ScienceDirect

Materials & Design

journal homepage: www.elsevier.com/locate/matdes

# Data-driven homogenisation of the response of heterogeneous ductile solids with isotropic damage

Weijian Ge, Vito L. Tagarielli *

*Department of Aeronautics, Imperial College London, SW72AZ London, UK*

ARTICLE INFO

*Keywords:*
Plasticity
Damage
Machine Learning
Data-driven
Constitutive Model

ABSTRACT

We propose a computational procedure to derive a data-driven surrogate constitutive model capturing the elastic–plastic response and progressive damage of a heterogeneous solid. This is demonstrated by analysing the response to deformation of a volume element of a non-linear, n-phase random composite, used in this study as a model material. Finite Element simulations are conducted, imposing pseudo-random, multiaxial, non-proportional histories of macroscopic strain to such volume element. The corresponding predicted histories of macroscopic stresses and other variables are recorded, to form part of a training dataset for the surrogate model. Essential additional training data is obtained by recording the changes in the homogenised stiffness matrix of the volume element during the deformation, by performing a series of linear perturbation analyses. Supervised machine learning is applied to the data, proposing suitable sets of inputs and outputs and implementing a phenomenological constitutive model based on simple neural networks. This results in a data-driven model of high accuracy.

## 1. Introduction

Damage refers to the gradual decline in mechanical stiffness that occurs during deformation of a solid. Continuum Damage Mechanics (CDM) provides a practical framework for modelling the initiation and progression of damage, by inclusion of damage parameters and rules to compute their evolution [1]. Often damage accompanies plasticity, for example in large deformation of polymeric and metallic materials [2].

Theoretical constitutive models for the plasticity and damage of solids typically assume that mechanical properties are uniform. However the presence of intrinsic heterogeneity in the microstructure of all solids [3] can play a significant role in the macroscopic mechanical response of the material [4]. To incorporate microscopic information into macroscopic models, several researchers have performed multiscale analyses [5–8] exploring the mechanical response of detailed representative volume elements (RVEs) modelling the materials of interest. This is insightful but computationally costly, which provides an opportunity to apply machine learning. Several authors have explored the integration of machine learning with continuum damage mechanics. A large portion of the existing research in this domain is dedicated towards parameter identification for predefined models. These studies have notably enriched experimental damage mechanics, providing frameworks for interpreting and predicting damage phenomena, however their reliance on theoretical assumptions significantly limits their flexibility [9–12] To address this limitation, increased research efforts have being directed towards data-driven surrogate models with minimal a priori assumptions on the material's response. Schowtjak et al. [13] proposed a model to chart the evolution of ductile damage in terms of void fractions using Artificial Neural Networks (ANN); Gerlach et al [14] introduced a model aimed at predicting the void area fraction in dual-phase steel, yielding quantitatively accurate predictions of the void area fraction across a variety of tensile and bending tests. Nguyen [15] exploited time series algorithms embedded within a deep learning framework to forecast crack growth in three-dimensional hydraulic fracturing problems. Fontes and Shadmehri [16] also made a notable contribution by proposing a data-driven model aimed at devising a failure model for Fiber-Reinforced Polymer (FRP) composite materials. Despite substantial progress, accurate predictions of the initiation and evolution of damage in heterogeneous materials under complex loading case are lacking. A computational framework to include data-driven models in multiscale simulations, free from theoretical assumptions and with sufficient flexibility to capture the response of arbitrary materials is also lacking. In this study we aim at filling this gap, presenting a new computational framework to assemble a training dataset and to

* Corresponding author.
*E-mail address:* v.tagarielli@imperial.ac.uk (V.L. Tagarielli).

https://doi.org/10.1016/j.matdes.2024.112738
Received 8 November 2023; Received in revised form 24 January 2024; Accepted 5 February 2024
Available online 9 February 2024
0264-1275/© 2024 The Author(s). Published by Elsevier Ltd. This is an open access article under the CC BY license (http://creativecommons.org/licenses/by/4.0/).

implement an accurate data-driven constitutive model of negligible computational cost, able to predict the plasticity and loss of cohesion of an arbitrary solid, and designed to be used in effective multiscale simulations. We demonstrate this framework on an isotropic model material with isotropic damage.

Homogenisation of a solid displaying softening behaviour can be problematic in multiscale material models, if not used within a stochastic framework, due to the accompanying strain localisation. In this work we therefore aim at predicting the response up to the onset of macroscopic softening.

We analyse a volume element (VE) in which the heterogeneity of the material is modelled through statistical descriptions of the mechanical properties, as in [17,18], and we homogenise the response of one single realisation of such VE. We then apply machine learning to develop a data-driven phenomenological model. The proposed procedure finds direct applications in multiscale simulations: given a representative volume element (RVE) modelling a material of interest (displaying an elastic–plastic response with accompanying progressive damage), the proposed procedure can effectively copy the RVE's response and reproduce it at negligible cost. For particularly complicated microstructures, for which an RVE needs to be meshed by millions of finite elements, the proposed procedure offers computational savings of several orders of magnitude without considerable loss of accuracy.

The paper is organized as follows. In Section 2 we explain the details of the FE simulations conducted and the strategy for assembling a suitable training dataset. Section 3 presents the supervised machine learning model and Section 4 discusses the accuracy of the data-driven surrogate model.

## 2. Production of a training dataset

The training data for the surrogate model refers to increments of deformation and to the evolution of several variables during such increments. We model the pseudo-random deformation of a n-phase random composite, idealised as a cubic array of $10 \times 10 \times 10$ identical cubes, or cells, each having randomly assigned Young's modulus, with all other properties being uniform and being modelled by a single finite element (FE) of type C3D8 in Abaqus [19]. The spatial distribution $E(x_i)$ of the modulus in the material is assumed to be

$$E(x_i) = E_{\min} + r_i(E_{\max} - E_{\min}) \tag{1}$$

where $r_i \in [0,1]$ represents random numbers of uniform probability density generated at the position of each cell, $x_i$, $i = 1, 2, \ldots N$. In this study it was assumed $E_{\min} = 150$ GPa, $E_{\max} = 450$ GPa, giving a relative variance of 100 %.

The choice of an uncorrelated, uniform probability density for the mechanical properties of each phase of the composite was based on the ease of implementation. The choice of introducing heterogeneity, in this study, only on the local Young's modulus, is based on the fact, observed in our previous study [20], that heterogeneity in this material property had a prominent effect on the macroscopic yield behaviour of the VE (for example when compared to introducing spatial heterogeneity in yield strength). The procedure in the present paper can be replicated with any prescribed statistical variation of any of the material properties, and the case of a randomly varying Young's modulus is chosen here as an example to illustrate the computational framework. The model solid considered here is not intended to represent the response of any real material, but is designed to display a relatively complex damage evolution, which we aim to capture with a surrogate model, which is the focus of this study.

### 2.1. Local (microscopic) constitutive model

To model the ductile damage response of each cell in the VE, we use the ductile damage model readily available in Abaqus [19]. The qualitative response of this model is illustrated in Fig. 1 in a uniaxial stress scenario. Prior to the yield point $\sigma_0$, the material exhibits linear elastic behaviour with a Young's modulus $E$ and Poisson's ratio $\nu$, followed by J2 von Mises plasticity, with isotropic hardening prescribed by the user. Damage initiation occurs at a stress $\sigma_{y0}$ and corresponding plastic strain $\bar{\varepsilon}_0^{pl}$, which is specified as a function of stress triaxiality. Following damage initiation, a single scalar damage variable $D$ is used to define the effective stress and stiffness as

$$\sigma = (1 - D)\bar{\sigma} \tag{2}$$

where $\bar{\sigma}$ is the stress in absence of damage, and

$$E(D) = (1 - D)E_0 \tag{3}$$

where $E_0$ is the initial elastic modulus. The damage variable $D$ evolves as a user-prescribed function of the local equivalent von Mises plastic strain $\bar{\varepsilon}^{pl}$ until this reaches a value of $\bar{\varepsilon}_f^{pl}$, when the damage parameter $D$ attains a value of 1. In 3D, for an isotropic material with stiffness matrix $\boldsymbol{C}$, it is

$$\boldsymbol{\sigma} = \boldsymbol{C}\boldsymbol{\varepsilon}^{el} = (1 - D)\boldsymbol{C}_0\boldsymbol{\varepsilon}^{el} \tag{4}$$

where $\boldsymbol{\varepsilon}^{el}$ is the elastic strain, obtained by the additive decomposition $\boldsymbol{\varepsilon} = \boldsymbol{\varepsilon}^{el} + \boldsymbol{\varepsilon}^{pl}$, and $\boldsymbol{C}_0$ is the initial elastic stiffness matrix.

The choice of isotropic local damage and of its evolution is made in this paper to aid clarity of the presentation, however the general procedure presented here is also applicable to solids with anisotropic yield and damage.

The material plasticity is defined as incompressible and rate independent, with isotropic linear hardening with strain hardening given by $\dot{\bar{\varepsilon}}^{pl} = \dot{\bar{\sigma}}/H$, where $H$ is a constant hardening modulus, and

$$\bar{\sigma} = \sqrt{\frac{3}{2}\boldsymbol{\sigma}^{dev} : \boldsymbol{\sigma}^{dev}}; \quad \bar{\varepsilon}^{pl} = \int_0^t \sqrt{\frac{2}{3}\dot{\boldsymbol{\varepsilon}}^{pl}\dot{\boldsymbol{\varepsilon}}^{pl}}\,dt \tag{5}$$

are the von Mises equivalent effective stress and accumulated equivalent plastic strain, respectively, such that $\boldsymbol{\sigma}\dot{\boldsymbol{\varepsilon}} = \bar{\sigma}\dot{\bar{\varepsilon}}^{pl}$, where $\boldsymbol{\sigma}^{dev}$ is the local deviatoric stress tensor, $\boldsymbol{\varepsilon}^{pl}$ is the local plastic strain tensor.

The damage initiation is assumed, in this model, to depend on the equivalent plastic strain and stress triaxiality. The equivalent plastic strain at the onset of damage $\bar{\varepsilon}_D^{pl}(\eta)$ is defined by the user as a function of stress triaxiality $\eta$, intended as the ratio of hydrostatic to von Mises stresses. In presence of variable triaxiality, the damage initiates when

$$\int \frac{d\bar{\varepsilon}^{pl}}{\bar{\varepsilon}_D^{pl}(\eta)} = 1 \tag{6}$$

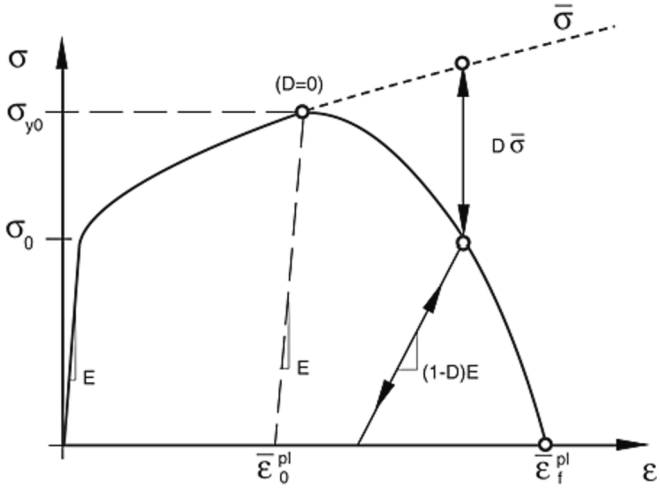



**Fig. 1.** Illustration of the local ductile damage response.

For simplicity the evolution of the damage parameter $D$ following damage initiation is taken in this study to be linear with the plastic displacement, as

$$\dot{D} = \frac{\dot{\bar{\varepsilon}}^{pl}}{\bar{\varepsilon}_f^{pl}} \tag{7}$$

where $\bar{\varepsilon}_f^{pl}$ is the equivalent plastic strain at failure. The damage evolution is inputted by tabulating the damage parameter as a function of the equivalent plastic displacement $\bar{u}^{pl} = L_e\left(\bar{\varepsilon}^{pl} - \bar{\varepsilon}_D^{pl}\right)$, where $L_e$ is the length of the cubic FE used (constant and uniform in this study).

Some of the mechanical properties defining the random material are listed in Table 1. The plastic strain at damage initiation depends on stress triaxiality according to the curve indicated as "micro" in Fig. 2. This dependency is chosen to give realistic strains for damage initiation and a tension/compression asymmetry, as observed in many different materials.

### 2.2. Loading of the VE

To generate simulation data, we impose on the VEs pseudo-random histories of macroscopic deformation. These are intended, in true strain space, as the histories of the components of the vector $\boldsymbol{\varepsilon} = [\varepsilon_{xx}, \varepsilon_{yy}, \varepsilon_{zz}, \varepsilon_{xy}, \varepsilon_{xz}, \varepsilon_{yz}]$. The histories are terminated upon meeting the condition $\sqrt{\varepsilon_{xx}^2 + \varepsilon_{yy}^2 + \varepsilon_{zz}^2 + \varepsilon_{xy}^2 + \varepsilon_{xz}^2 + \varepsilon_{yz}^2} \geqslant \varepsilon_{\max}$ and comprise multiple steps, of fixed time duration $\Delta t$ (note: such loading steps are not to be confused with the simulation increments). In each of these time steps, each component of macroscopic strain is updated by an amount

$$\Delta\varepsilon_i = sgn(r_1 - \theta)[\Delta\varepsilon_{\text{mini}} + r_2 \cdot (\Delta\varepsilon_{\text{maxi}} - \Delta\varepsilon_{\text{mini}})], \quad i = x, y, z, xy, xz, yz \tag{8}$$

where $\Delta\varepsilon_{\text{mini}}$, $\Delta\varepsilon_{\text{maxi}}$ are the minimum and maximum allowable amplitudes of the increment in each strain component, $r_1$ and $r_2$ are realisations of a uniform random variable between 0 and 1, and $\theta$ defines the probability that the amplitude of each strain step is negative (equal probability of positive and negative steps is assumed in this study, $\theta = 0.5$).

The strain histories obtained as above are then smoothed by a smoothing function. The time/strain pairs obtained via eq. (8) are used as seed points for the smoothing, and intermediate points between two consecutive seed points $(t_J, \varepsilon_J)$ and $(t_{J+1}, \varepsilon_{J+1})$, are interpolated as $\left(t, A_J + (A_{J+1} - A_i)\zeta^3(10 - 15\zeta + 6\zeta^2)\right)$, with $\zeta = (t - t_J)/(t_{J+1} - t_J)$.

We set $\varepsilon_{\max} = 0.1$, $\Delta\varepsilon_{\max} = 0.01$, $\Delta\varepsilon_{\min} = 0.005$ based on the results of preliminary studies. An example of the straining paths obtained with these parameters is illustrated in Fig. 3. In this study we use rate-insensitive constitutive models and therefore the numerical value of the time $t$ does not affect the stress versus strain histories produced. We note in passing that the smoothing function above can improve the distribution (variance) of strain rate data, which is important when rate-dependent constitutive models are used.

We choose this strategy to produce the training data due to its simplicity and effectiveness, which we had previously assessed [17]. In this study no effort is made to optimise the training dataset, but the sampling of data along the strain trajectories could be tuned to maximise some desired features, such as uniformity in input space density.

### 2.3. FE analyses

FE simulations were performed using Abaqus Explicit with adaptive time stepping and considering geometrical nonlinearity. The mass was rescaled to allow larger timesteps, and the magnitude of time was stretched to ensure that the kinetic energy in the simulations was a negligible fraction of the internal energy (considerably lower than 1 %). The choice of Explicit over Standard (implicit integration) was to ensure convergence of all analyses for a sufficient time to allow capturing the initial phase of macroscopic softening of the VE's response, in which Abaqus Standard simulations became occasionally unstable. For selected simulations we checked that the implicit and explicit solvers gave identical predictions; the use of Explicit was preferred due to its increased reliability when producing large amounts of training data.

The n-phase composites were meshed such that each phase corresponded with a single 8-noded finite element with full integration; this choice was to reduce the computational cost of the FE analyses on this model composite material.

Periodic boundary conditions were applied to the volume element. The reference body was a $L_x \times L_y \times L_z (1 \times 1 \times 1$ mm in this case) cuboid. Nodes on the boundary of the cuboid were split into three different sets representing individual faces, edges and vertices, and constraint equations were imposed on their displacement degrees of freedom as specified in [21].

The boundary $\partial\Omega$ of the VE was decomposed into two subsets $\partial\Omega^+$ and $\partial\Omega^-$, so that $\partial\Omega = \partial\Omega^+ + \partial\Omega^-$. Each point of the reference body

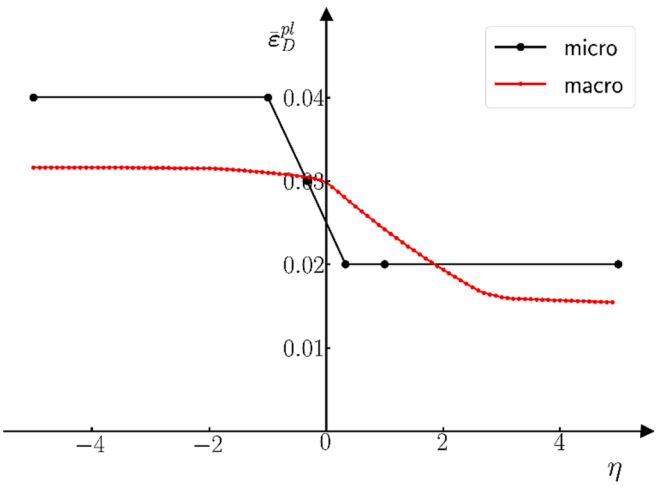



**Fig. 2.** The local (microscopic) and global (macroscopic) relation between $\eta$ and $\bar{\varepsilon}_D^{pl}$ at damage initiation.

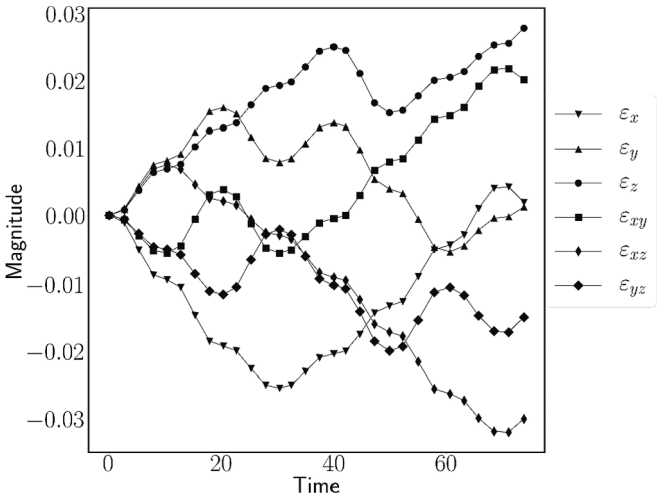



**Fig. 3.** An example of a 6D multi-axial straining history.

**Table 1**
Summary of the mechanical properties assumed in this study.

| |
|---|
| $E = 300$Gpa, $H = 2$Gpa, $\nu = 0.3$, $\sigma = 100$Mpa, $\bar{\varepsilon}_f^{pl} = 0.15$, $L_e = 0.1$mm |

$\boldsymbol{X}^+ \in \partial\Omega^+$ was paired by periodicity to a point $\boldsymbol{X}^- \in \partial\Omega^-$. The periodic boundary condition was then imposed such that:

$$\boldsymbol{x}^+ = \boldsymbol{x}^- + \boldsymbol{F}(\boldsymbol{X}^+ - \boldsymbol{X}^-) \tag{9}$$

where $\boldsymbol{x}^+$ and $\boldsymbol{x}^-$ are coordinates of $\boldsymbol{X}^+$, $\boldsymbol{X}^-$ after deformation and $\boldsymbol{F}$ is the macroscopic deformation gradient applied.

A large-strain description of the RVE's kinematics is convenient to perform and illustrate the calculation of the macroscopic Cauchy stress $\boldsymbol{\sigma}$ and true logarithmic strain $\boldsymbol{\varepsilon}$, which will be used to train the surrogate model, and for the extraction of the current stiffness matrix, which is described below. However in this study the imposed macroscopic strains never exceed a few percent and therefore a small strain formulation would be sufficient, and we will assume below that the logarithmic strain tensor, $\boldsymbol{\varepsilon}$, can be decomposes additively in macroscopic plastic and elastic strains.

For convenience of implementation, eq.(9) can be expressed in terms of displacement field $\boldsymbol{u}$

$$\begin{aligned}(\boldsymbol{x}^+ - \boldsymbol{X}^+) - (\boldsymbol{x}^- - \boldsymbol{X}^-) &= (\boldsymbol{F} - \boldsymbol{I})(\boldsymbol{X}^+ - \boldsymbol{X}^-)\\ \boldsymbol{u}^+ - \boldsymbol{u}^- &= (\boldsymbol{F} - \boldsymbol{I})(\boldsymbol{X}^+ - \boldsymbol{X}^-)\\ &= \begin{bmatrix} \frac{\partial u_x}{\partial X} & \frac{\partial u_x}{\partial Y} & \frac{\partial u_x}{\partial Z} \\ \frac{\partial u_y}{\partial X} & \frac{\partial u_y}{\partial Y} & \frac{\partial u_y}{\partial Z} \\ \frac{\partial u_z}{\partial X} & \frac{\partial u_z}{\partial Y} & \frac{\partial u_z}{\partial Z} \end{bmatrix} (\boldsymbol{X}^+ - \boldsymbol{X}^-)\end{aligned} \tag{10}$$

(with the subscripts $+$ and $-$ referring to the domains $\partial\Omega^+$ and $\partial\Omega^-$.) To control the imposed macroscopic deformation, 3 reference points RP1, RP2, RP3, each with 3 Degrees of Freedom (DOF), are created. We define the input tensor $\boldsymbol{U}$ such that its component $U_{ij}$ indicates the j-th DOF imposed onto the i-th reference point. These components are interpreted as

$$\begin{aligned} U_{1,1} &= \frac{\partial u_X}{\partial X}, U_{1,2} = \frac{\partial u_Y}{\partial Y}, U_{1,3} = \frac{\partial u_Y}{\partial Y} \\ U_{2,1} &= \frac{\partial u_Y}{\partial X}, U_{2,2} = \frac{\partial u_Z}{\partial X}, U_{2,3} = \frac{\partial u_Z}{\partial Y} \\ U_{3,1} &= \frac{\partial u_X}{\partial Y}, U_{3,2} = \frac{\partial u_X}{\partial Z}, U_{3,3} = \frac{\partial u_Y}{\partial Z} \end{aligned} \tag{14}$$

The true strain histories, such as those in Fig. 3, are converted in histories of the components of the deformation gradient $\boldsymbol{F}$ using

$$\boldsymbol{\varepsilon} = \ln(\boldsymbol{F}) = \sum_{i=1}^{3} \ln\lambda_i \boldsymbol{N}_i \otimes \boldsymbol{N}_i \tag{15}$$

where $\lambda_i$ are the principal stretches and $\boldsymbol{N}_i$ the principal stretch directions.

During the simulation we record the reaction forces (RF) at the reference points and we obtain the nominal stress $\boldsymbol{P}$ as

$$\boldsymbol{P} = \begin{bmatrix} \mathrm{RF}_{1,1}/A_x & \mathrm{RF}_{2,1}/A_x & \mathrm{RF}_{2,2}/A_x \\ \mathrm{RF}_{3,1}/A_y & \mathrm{RF}_{1,2}/A_y & \mathrm{RF}_{2,3}/A_y \\ \mathrm{RF}_{3,2}/A_z & \mathrm{RF}_{3,3}/A_z & \mathrm{RF}_{1,3}/A_z \end{bmatrix} \tag{16}$$

where $A_x = L_yL_z, A_y = L_xL_z, A_z = L_xL_y$. The true Cauchy stress tensor is then calculated as

$$\boldsymbol{\sigma} = \boldsymbol{F}\cdot\boldsymbol{P}/\det(\boldsymbol{F}) \tag{17}$$

The use of true stress and strain ensures objectivity of these quantities, which will be used to formulate the surrogate constitutive model. The objectivity of the constitutive relation can be enforced at the moment of its implementation in a FE material subroutine, by correcting the stress measure in presence of rigid body rotations (which were absent in the data generated here for training the surrogate model).

### 2.4. Measurement of the current stiffness matrix of the VE

Quantitative data on the evolution (degradation) of the stiffness of the VE with continued random deformation is needed to inform our data-driven model. During all FE analyses we therefore extract, at selected times, the current stiffness matrix of the material. Knowledge of the current macroscopic stiffness matrix is necessary for the homogenisation of the material's response, which with continued strain will display a progressive loss of macroscopic stiffness. The surrogate model will be trained to compute the change in stiffness matrix over a simulation increment, starting from knowledge of such matrix at the beginning of the increment. The measurement of the stiffness is done as follows.

Similar to[22], at the time of interest $t$ we record the deformed coordinates of the nodes, the initial local stiffness matrices $\boldsymbol{C}_{1\ldots m}(0)$ and the local damage variables $D_{1\ldots m}(t)$ of all the $m$ integration points. A secondary FE model is then built, with nodes and elements corresponding to the deformed configuration of the primary simulation at time $t$, and elastic stiffness distributed as $\boldsymbol{C}_{1\ldots m}(t) = [1 - D_{1\ldots m}(t)]\boldsymbol{C}_{1\ldots m}(0)$ over the integration points. The secondary FE model, which is purely elastic and does not account for plasticity or damage, is then subjected to a set of 6 simulations, each prescribing a small variation in one macroscopic strain component, while keeping the other 5 components constrained to vanish. This is necessary to assemble the stiffness matrix and it is performed as follows.

Consider that at the selected time $t$, in the primary simulation the VE has undergone deformation

$$\boldsymbol{x}_0 = \boldsymbol{F}_0\boldsymbol{X} \tag{18}$$

where $\boldsymbol{F}_0$ is the deformation gradient. This corresponds to imposed displacements of the reference points given by

$$\boldsymbol{u}_0^+ - \boldsymbol{u}_0^- = (\boldsymbol{F}_0 - \boldsymbol{I})(\boldsymbol{X}^+ - \boldsymbol{X}^-) \tag{19}$$

In the secondary FE simulations identical periodic boundary conditions as in the primary simulation are imposed. In these simulations we start from the reference configuration $\boldsymbol{x}_0$ and we apply an additional deformation gradient $\boldsymbol{F}_\gamma$, reaching the configuration $\boldsymbol{x}_\gamma$

$$\boldsymbol{x}_\gamma = \boldsymbol{F}_\gamma\boldsymbol{x}_0 = \boldsymbol{F}_\gamma\boldsymbol{F}_0\boldsymbol{X} \tag{20}$$

In terms of displacements of the reference points

$$\boldsymbol{u}_\gamma^+ - \boldsymbol{u}_\gamma^- = (\boldsymbol{F}_\gamma\boldsymbol{F}_0 - \boldsymbol{I})(\boldsymbol{X}^+ - \boldsymbol{X}^-) \tag{21}$$

Appropriate displacements $\boldsymbol{U}_\gamma - \boldsymbol{U}_0$ are applied, imposing in turn a single macroscopic strain component (of small numerical value) in the secondary FE simulations; the corresponding reaction forces are used to calculate the nominal stress $\boldsymbol{P}$, as above. The columns of $\boldsymbol{P}$, divided by the magnitude of the small strain applied, represent the corresponding columns of the current stiffness matrix.

The current stiffness matrix is expressed in terms of true stresses and strains. Due to the small strains imposed in the linear analyses, the Cauchy stress can be calculated as $\boldsymbol{\sigma} = \boldsymbol{F}_0\cdot\boldsymbol{P}/\det(\boldsymbol{F}_0)$.

To reduce the computational cost for the production of a training database, the extraction of the current stiffness $\boldsymbol{C}(t)$ is performed in this study at a frequency of 1 Hz, and the values of $\boldsymbol{C}(t)$ between two direct measurements are linearly interpolated according to time.

### 2.5. Construction of the training database

The primary FE simulations are non-linear in geometry and material response, therefore the FE solutions are incremental. A datapoint of our training database is represented by one increment in these simulations. We note that the time duration of the increments can be adjusted by the

user; in this study, it was set to 10 s. Several random strain histories are applied to our VE (starting from a stress-, strain- and damage-free configuration), and the corresponding evolution of stress, strain as well as the plastically dissipated energy $W^{pl}$, the damage-dissipated energy $W^{D}$ and the current macroscopic stiffness matrix $\boldsymbol{C}$. We assume that additive strain decomposition applies to macroscopic quantities, such that the macroscopic plastic strain components can be calculated as

$$\boldsymbol{\varepsilon}^{pl} = \boldsymbol{\varepsilon} - \boldsymbol{\varepsilon}^{el} = \boldsymbol{\varepsilon} - \boldsymbol{\sigma}/\boldsymbol{C} \tag{22}$$

We then consider all increments in the FE simulations and compute the variation of all the above quantities as well as the macroscopic von Mises equivalent plastic strain and its accumulated value in the current random strain history

$$\Delta\bar{\varepsilon}^{pl} = \sqrt{\frac{2}{3}\Delta\boldsymbol{\varepsilon}_j^{pl}\Delta\boldsymbol{\varepsilon}_j^{pl}}, \bar{\varepsilon}^{pl} = \int_0^t \frac{\Delta\dot{\bar{\varepsilon}}^{pl}}{\Delta t}\,dt \tag{23}$$

To develop a data-driven model of suitable accuracy, we simulated the response of the VE to a set of 330 different random strain histories, 300 of which were used for training, while 30 were used for testing on unseen data. The initial stiffness of the VE, $\boldsymbol{C}_0$, is given below as

$$\boldsymbol{C}_0 = \frac{E_0}{1-\nu^2}\begin{bmatrix} 1 & 0.44 & 0.44 & & & \\ 0.44 & 1 & 0.44 & & & \\ 0.44 & 0.44 & 1 & & & \\ & & & 0.29 & & \\ & & & & 0.29 & \\ & & & & & 0.29 \end{bmatrix} \tag{24}$$

As expected (and confirmed in [17]), the effective elastic material behaviour is close to isotropic, with the expected symmetries ($C_{11} \approx C_{22} \approx C_{33}$, $C_{12} \approx C_{13} \approx C_{23}$, $C_{44} \approx C_{55} \approx C_{66}$) and negligible values of the terms coupling direct and shear strains.

### 2.6. Homogenised damage response

Upon imposing macroscopic strain histories, the stiffness matrix evolved. An example of such evolution for a selected random strain history is presented in Fig. 4. We observe that the components $C_{11}$, $C_{12}$ and $C_{44}$ initially remain unchanged and then decrease as damage is initiated. When normalised by their initial values, these components show identical relative degradation histories, confirming that the macroscopic damage behaviour of the VE is isotropic, and can be therefore characterised by a single scalar damage parameter. Mathematically, we define the macroscopic (homogenised) damage parameter $d(t)$ as

$$d(t) = 1 - \frac{C_{11}(t)}{C_{11}(0)} \approx 1 - \frac{C_{ij}(t)}{C_{ij}(0)} \tag{25}$$

i.e. in the following the macroscopic damage will be quantified by the ratio $C_{11}(t)/C_{11}(0)$. The energy dissipated as a result of damage can be computed as

$$W_d = \int_0^t \int_V \frac{\dot{d}}{2(1-d)}\boldsymbol{\sigma} : \boldsymbol{\varepsilon}^{el} dV d\tau = \\ = \sum_{j=1}^{n} \frac{\Delta d_j}{2(1-d_j)}\boldsymbol{\sigma}_j : \boldsymbol{\varepsilon}_j^{el} \tag{26}$$

where $V$ is the volume of the VE, $j$ is an index to sum over all the $n$ phases of the composite.

The comparison of this prediction with FE outputs, shown in Fig. 5, reveals initially a very close match with an increasing minor deviation of the two curves. This discrepancy is not investigated further here; it could

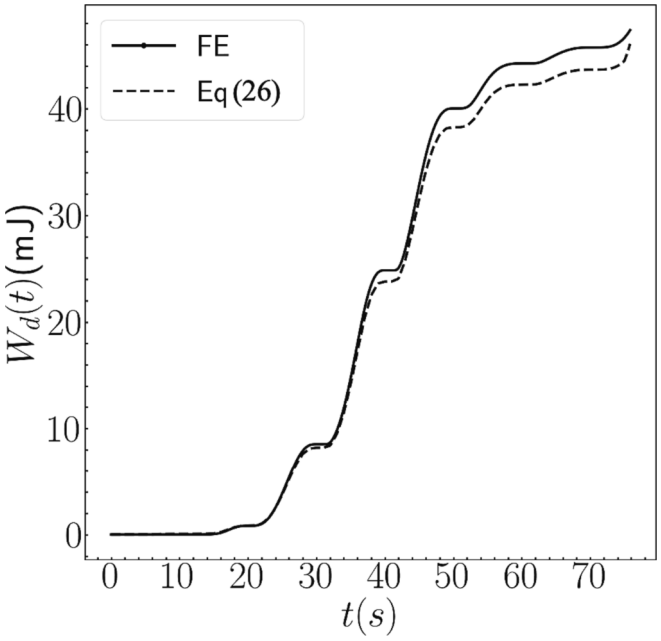



**Fig. 5.** Comparison between FE and theoretical predictions (eq. (26)) of the damage dissipation energy in a selected simulation.

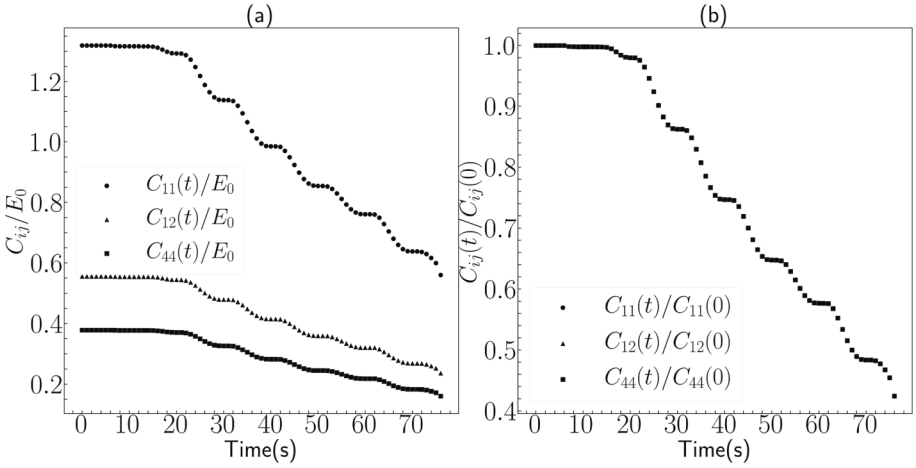



**Fig. 4.** An example of stiffness degradation during loading; (a) the decrease of three major components of the stiffness matrix; (b) the relative decrease of the same three components.

be attributed to the errors introduced by the linear interpolation of the current stiffness matrix or to the inherent limitations in the homogenization of plastic strains, as discussed in [23].

### 2.7. Instability and localisation

With continued applied deformation, eventually the VE displays a prominent and sudden decrease in macroscopic stress and stiffness. Microscopically this is linked to the localization of strain, as in the example shown in Fig. 6. Numerical computational homogenization frameworks of softening responses is considered problematic due to concerns about representativeness [24–26]. Here we only model the material response before the onset of instability. To identify the point of instability we apply Hill's criterion [27], i.e. that a body is stable if

$$\int_V \dot{\sigma}_{ij}\dot{\varepsilon}_{ij}dV > 0 \tag{27}$$

In each simulation we mark the time when an increment is first detected where eq. (27) is not met, and we discard the subsequent data for the purpose of training of the surrogate model, leaving the formulation of a model for the softening response to future research. Fig. 7 shows an example of the detection of incipient instability in a selected simulation.

## 3. Data-driven surrogate model

The proposed model is composed of different sub-models: a classification model, two regression models, and a damage initiation model. These parts form a framework to predict increments in macroscopic stress, damage variable and other parameters for a given increment in strain. In all sub-models supervised machine learning is applied by employing simple multilayer feed-forward neural networks, all with a single output $y$, two hidden layers having 100 neurons each, both using the activation function $\boldsymbol{ReLu}(\alpha) = \max(0, \alpha)$. Minimisation of all loss functions is achieved by stochastic back-propagation, using the Adam algorithm with no regularisation, a maximum of 3000 epochs, a batch size of 50 and learning rate of 0.001. The choice of these parameters was made based on the result of a preliminary study aimed at maximising accuracy while maintaining a reasonable computational cost. All neural networks used in this study could be optimised to increase the accuracy and the speed of the surrogate model, and different types or regressions (different from NN) could also be considered. Here the model is limited to NNs of fixed structure and hyperparameters, to place the focus on the physical information to include in the surrogate model, rather than on the specific machine learning techniques.

The neural networks $\boldsymbol{NN}(\boldsymbol{x})$ used in this study have the structure

$$y = NN(\boldsymbol{x}) = \boldsymbol{W_2 ReLu}(\boldsymbol{W_1}(\boldsymbol{ReLu}(\boldsymbol{W_0 x} + \boldsymbol{b_0})) + \boldsymbol{b_1}) + \boldsymbol{b_2} \tag{28}$$

where $\boldsymbol{W}_0$, $\boldsymbol{W_1}$, $\boldsymbol{W}_2$ are weight matrices and $\boldsymbol{b}_0$, $\boldsymbol{b_1}$, $\boldsymbol{b}_2$ are column vectors of biases,$\boldsymbol{x}$ is the input vector.

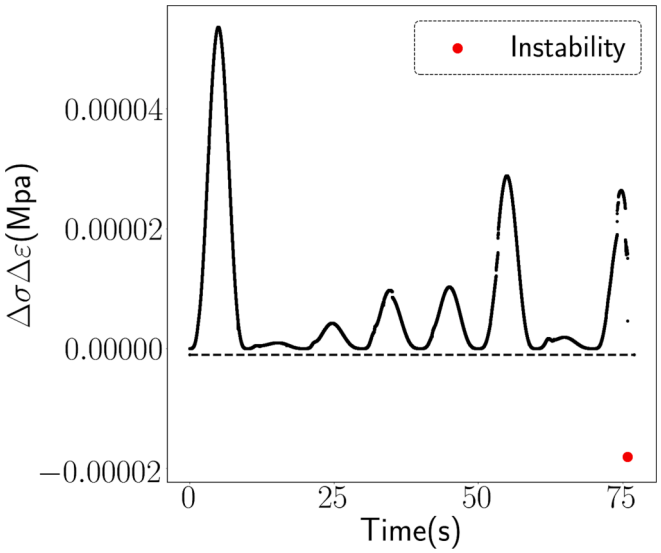



**Fig. 7.** An example of instability detection by application of Hill's criterion.

A 90 % fraction of the training datapoints were randomly selected to train the NNs and the remaining 10 % served as validation data. The training data coordinates were normalized by subtracting their average and dividing by their variance. The training was carried out by a back-propagation algorithm, using stochastic gradient descent with adaptive moment estimation. The batch size was set to 50, the learning rate was 0.001, and early stopping was employed to halt the training if the validation loss did not decrease for 100 consecutive epochs.

### 3.1. Classification model

This model classifies a simulation increment as elastic or plastic. We recall that in the microscopic constitutive model, damage initiation occurs after the initiation of plastic deformation. A subset of $\phi$ training datapoints was randomly selected among those with damage not yet initiated ($W_d = 0$) to have an equal number of increments with and without plasticity. The subset was categorized into these two groups by a label $y$

$$y = \begin{cases} 0 & if\ \Delta W_{pl} = 0\ (\text{elastic}) \\ 1 & if\ \Delta W_{pl} > 0\ (\text{inelastic loading}) \end{cases} \tag{29}$$

In this classification we assume that current strain and strain increment are sufficient to determine the value of the label, i.e.

$$y = NN_{clas}\left(\boldsymbol{\varepsilon}^{el}, \Delta\boldsymbol{\varepsilon}\right) \tag{30}$$

We note that knowledge of the elastic strain is equivalent to knowledge

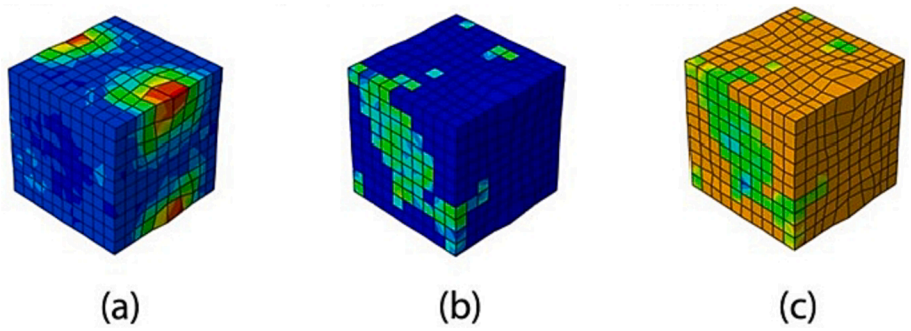



**Fig. 6.** Example of the localisation of (a) maximum principal strain (blue: 0; red: 0.77); (b) stress (blue: 0; red: 245 MPa), and (c) damage parameter $D$ (orange: 0.44; green: 0.95). (For interpretation of the references to colour in this figure legend, the reader is referred to the web version of this article.)

of the stress at the beginning of the increment, as the current stiffness of the VE is known. We therefore assume that knowledge of the initial stress and of the strain increment is sufficient to predict if an increment will be inelastic; this assumption is not completely consistent from the energetic point of view but it was found effective, as it will be shown below.

The loss function is defined as the *binary cross entropy*

$$H(\boldsymbol{x}) = \frac{-1}{\phi}\sum_{j=1}^{\phi}\left(y^j_{label}\ln\left(\widehat{y}^j\right) + \left(1-y^j_{label}\right)\ln\left(1-\widehat{y}^j\right)\right) \tag{31}$$

where $\widehat{y}^j$ are the predicted values of the label according to the neural network and $y^j_{label}$ are the corresponding true values of the label.

### 3.2. Regressions to predict $\Delta\boldsymbol{\varepsilon}^{pl}$ and $\Delta d^M$

To predict the values of the increment in macroscopic plastic strain $\Delta\boldsymbol{\varepsilon}^{pl}$ and macroscopic damage variable $\Delta d^M$, two separate regression models are established. Both have a loss function defined as the mean absolute error (*MAE*)

$$MAE = \frac{1}{\overline{\phi}}\sum_{j=1}^{\overline{\phi}}\sum_{k=1}^{\beta}\left|y^j_k - \widehat{y}^j_k\right| \tag{32}$$

where $\widehat{y}^j_k$ are predictions of the NN and $y^j_k$ the true values ($\beta$ is the length of the vector $\boldsymbol{y}$,$\overline{\phi}$ is the number of the testing datapoints). For the prediction of $\Delta\boldsymbol{\varepsilon}^{pl}$, we assume

$$\Delta\boldsymbol{\varepsilon}^{pl} = NN^{pl}_{reg}\left(\boldsymbol{\varepsilon}^{el},\boldsymbol{\varepsilon}^{pl},\overline{\varepsilon}^{pl},\Delta\boldsymbol{\varepsilon}\right) \tag{33}$$

as this choice proved effective in our previous studies on elastic–plastic materials [17]. We note that knowledge of $\boldsymbol{\varepsilon}^{el}$ and $\boldsymbol{\varepsilon}^{pl}$ is equivalent to knowledge of the initial stress and strain, due to knowledge (in this study) of the current stiffness and to the assumed additive strain decomposition. In physical terms, we assume that all effects of the previous deformation history are represented effectively by the initial macroscopic stress and strain states and by the accumulated von Mises equivalent plastic strain $\overline{\varepsilon}^{pl}$.

To predict the increment of the macroscopic damage variable, a regression model was constructed, using data points with a non-zero increment in energy dissipated by damage. We assume that the increment in macroscopic damage depends on the initial damage (known from knowledge of the current stiffness matrix of the VE), on the increment in plastic strain and on the accumulated von Mises plastic strain, i.e.

$$\Delta d^M = NN^{dm}_{reg}(\overline{\varepsilon}^{pl}, d^M, \Delta\boldsymbol{\varepsilon}^{pl}) \tag{34}$$

This partially mimics the response of the material at a microscopic level.

### 3.3. Model for damage initiation

An additional component of the proposed computational framework is a model to predict the initiation of macroscopic (homogenised) damage $d$, intended as the point of incipient degradation of the macroscopic stiffness matrix. The local constitutive model assumes that the initiation of damage depends on the applied plastic strain and stress triaxiality. At the macroscopic level we make the same assumption, due to its simplicity and effectiveness. We therefore seek a function providing the macroscopic equivalent plastic strain at damage initiation $\overline{\varepsilon}^{pl}_d$ as a function of the macroscopic stress triaxiality $\eta$, and use a NN to represent this function, as

$$\overline{\varepsilon}^{pl}_d(\eta) = NN^{init}_{reg}(\eta) \tag{35}$$

To construct the training data for $NN^{init}_{reg}(\eta)$ we collect, along all random strain histories used to generate the training database, histories of homogenised triaxiality $\eta_j$ and plastic strain increment $\Delta\overline{\varepsilon}^{pl}_j$ until the initiation of damage (and excluding the point of damage initiation). Mimicking the structure of eq. (6), we define the loss function for this training as

$$\begin{aligned} loss &= \frac{1}{m}\sum_{k=1}^{m}|\omega_k - 1| \\ &= \frac{1}{m}\sum_{k=1}^{m}\left|\sum_j \frac{\Delta\overline{\varepsilon}^{pl}_j}{NN^{init}_{reg}(\eta_j)} - 1\right| \end{aligned} \tag{36}$$

where $m$ denotes the total number of random strain histories and $j$ is a chronological index ordering datapoints along each random strain history.

### 3.4. Overall computational framework

We now describe how the previous sub-models are integrated to develop the data-driven constitutive model; this is a function providing the increment in macroscopic stress as a function of an arbitrary imposed strain increment and other state variables. The framework is summarised in Fig. 8.

First, the classification model is applied to determine if an increment is elastic or plastic. We assume additive strain decomposition applies; when the material is in the elastic region the strain is updated as

$$\boldsymbol{\varepsilon}^{el}_{n+1} = \boldsymbol{\varepsilon}^{el}_n + \Delta\boldsymbol{\varepsilon}_n \tag{37}$$

where the index $n$ indicates the current increment number. After the material has yielded, as determined by the classification, we predict the increment of the plastic strain using the neural network $NN^{pl}_{reg}$ and update elastic and plastic strains, as well as the accumulated von Mises plastic strain, i.e.

$$\Delta\boldsymbol{\varepsilon}^{pl}_n = NN^{pl}_{reg}\left(\boldsymbol{\varepsilon}^{el}_n,\boldsymbol{\varepsilon}^{pl}_n,\overline{\varepsilon}^{pl}_n,\Delta\boldsymbol{\varepsilon}_n\right) \tag{38}$$

$$\begin{aligned} \boldsymbol{\varepsilon}^{el}_{n+1} &= \boldsymbol{\varepsilon}^{el}_n + \Delta\boldsymbol{\varepsilon}_n - \Delta\boldsymbol{\varepsilon}^{pl}_n \\ \boldsymbol{\varepsilon}^{pl}_{n+1} &= \boldsymbol{\varepsilon}^{pl}_n + \Delta\boldsymbol{\varepsilon}^{pl}_n \end{aligned} \tag{39}$$

$$\overline{\varepsilon}^{pl}_{n+1} = \overline{\varepsilon}^{pl}_n + \sqrt{\frac{2}{3}\Delta\boldsymbol{\varepsilon}^{pl}_n\Delta\boldsymbol{\varepsilon}^{pl}_n} \tag{40}$$

The cumulative damage variable $\omega_n$ defined similar as in eq. (6) is also updated as

$$\omega_{n+1} = \omega_n + \frac{\Delta\overline{\varepsilon}_n}{\overline{\varepsilon}^{pl}_D(\eta_n)} \tag{41}$$

For increments with $\omega_n \geqslant 1$, indicating that damage has initiated, the macroscopic damage variable is also updated, using the regression described above, as

$$d^M_{n+1} = d^M_n + NN^{dm}_{reg}\left(\overline{\varepsilon}^{pl}_n, d^M_n, \Delta\boldsymbol{\varepsilon}_n\right) \tag{42}$$

The stress is finally updated by multiplying the current stiffness matrix by the macroscopic elastic strain

$$\boldsymbol{\sigma}_{n+1} = (1-d^M_{n+1})\boldsymbol{C}_0\boldsymbol{\varepsilon}^{el}_{n+1} \tag{43}$$

The framework above is implemented in Python and it can be used to predict the evolution of state variables subject to arbitrary histories of imposed strain.

The data contained in the training dataset satisfy the first and second principles of thermodynamics, and as a result the surrogate model also satisfies these laws in 100 % of the increments. A preliminary study

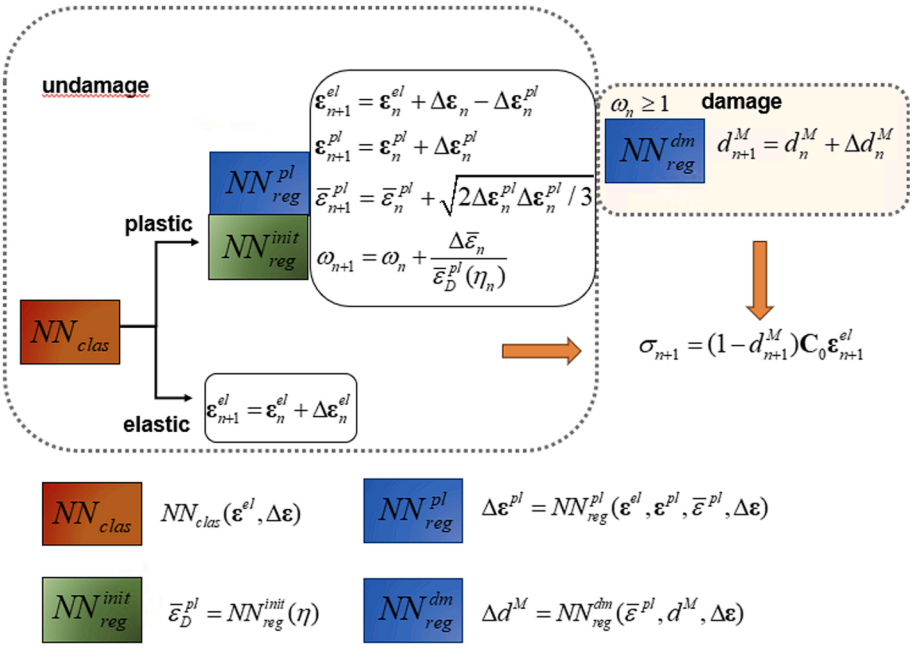



**Fig. 8.** Illustration of the proposed computational framework.

explored the effects of introducing constraint terms in the loss function to effectively enforce the first two principles of thermodynamics in the regressions, however no tangible improvements were observed when introducing such constraints. In this study the hyperparameters of the NN used are not optimised and it is possible that the thermodynamical constraints might introduce notable improvements in the training process if optimal NNs were used; this will be explored in future studies.

## 4. Results and discussion

We proceed to evaluate the performance of the model. We begin with the classification of elastic/inelastic increments. The neural network $NN_{clas}$ is trained by a dataset of 9688 datapoints. To evaluate its accuracy we perform 30 additional FE simulations of the response of the VE element to random strain histories; this represents a set of test datapoints in the form of simulation increments that were not included in the training database (unseen). The accuracy of the NN is illustrated in Fig. 9 in the form of a confusion map, which indicates that the classification model can distinguish between initial elastic and plastic increments effectively with an overall accuracy of 99.91 %.

To illustrate the accuracy of the two regressions performed, we examine the loss function of the NNs (*MAE* for both). Fig. 10 presents, for the networks predicting increments in plastic strain and damage variable, the sensitivity of the final loss functions to the number of training datapoints. Increasing the number of training data points leads to a reduction in MAE for both models, although this is not strictly monotonic. Increasing the size of the training dataset can improve the accuracy of the regressions.

The network $NN_{reg}^{init}$, predicting the initiation of damage, is assessed by quantifying the relative time difference between the predicted and actual damage initiation, by the parameter

$$\delta = \frac{|\hat{t}_{init} - t_{init}|}{T} \tag{44}$$

where $\hat{t}_{init}$ denotes the predicted damage initiation time, $t_{init}$ denotes the actual damage initiation time and $T$ is the total time duration of the imposed random strain history. Fig. 11 presents the dependency of $\bar{\delta}$, the average of $\delta$ computed over 30 unseen random strain histories, on the number of random strain histories used to train the model. The trend is

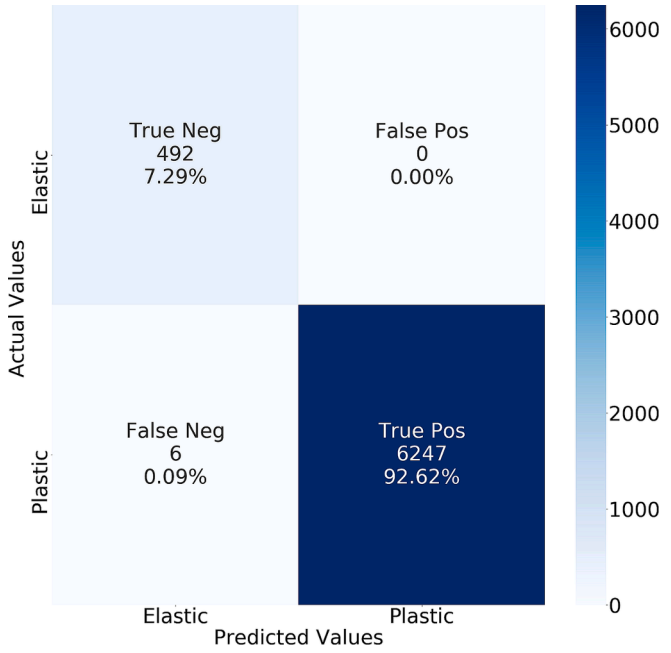



**Fig. 9.** Confusion matrix showing the performance of the classification model.

not monotonic; the percent error in predicting the time at damage initiation is comprised between 1 % and 2 % irrespective of the data used for training. An optimal performance is obtained when using 100 random strain histories to train $NN_{reg}^{init}$.

We also compute the dependency of the macroscopic plastic strain at damage initiation upon macroscopic stress triaxiality, shown in Fig. 2. The comparison between microscopic and macroscopic responses highlights effectively the effects of material heterogeneity on the macroscopic damage response of the VE, promoting lower strains at damage initiation than those at the microscopic level.

We now proceed to evaluate the combined performance of the sub-models examined above. We test the accuracy of the model when predicting the homogenised material response when the VE is subject to 30

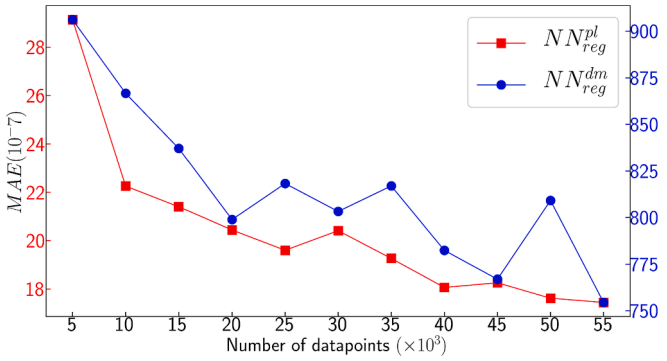



**Fig. 10.** Effect of the size of training dataset on the loss functions of the NNs predicting increments in plastic strain and damage variables.

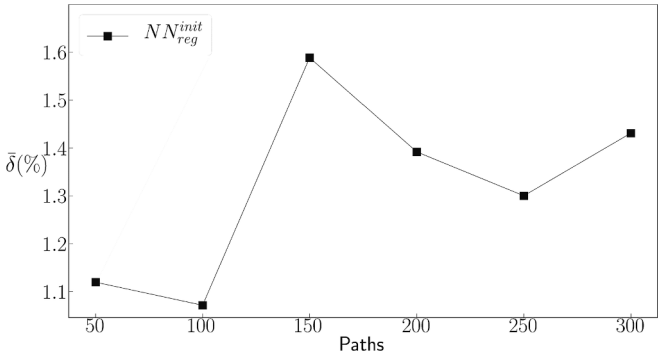



**Fig. 11.** Accuracy of the damage initiation prediction $\bar{\delta}$ as a function of the number of random strain histories used for training.

unseen imposed histories of macroscopic strain. The results presented below were obtained combining the neural networks described above with the following settings: $NN_{clas}$ was trained with 9688 classification datapoints, $NN^{pl}_{reg}$ and $NN^{dm}_{reg}$ with 55,000 datapoints, and $NN^{init}_{reg}$ trained with 100 datapoints. To measure the accuracy of the predictions, we compare pairs of expected and predicted stress versus strain curves by using the metric $E_{\sigma}$

$$E_{\sigma} = \frac{1}{N_{inc}} \sum_{j=2}^{N_{inc}} \left( \frac{\left\| \boldsymbol{\sigma}_j^{NN} - \boldsymbol{\sigma}_j^{FE} \right\|_2}{\left\| \boldsymbol{\sigma}_j^{NN} \right\|_2} \right) \tag{45}$$

where $\boldsymbol{\sigma}_j^{FE}$ is the expected macroscopic stress at a given strain and $\boldsymbol{\sigma}_j^{NN}$ is the corresponding prediction of the surrogate model. $E_{\sigma}$ is dependent on the length of the strain trajectory considered and on the density of simulation increments along these trajectories. The generation of training data used in this study implies a relatively small density of data near the end of the strain histories (which occurs either at the termination strain $\varepsilon_{\max}$ or at the onset of instability, if this occurs). The incremental nature of these predictions also implies that the error tends to accumulate with continued deformation.

In Figs. 12 and 13 we assess the accuracy of the surrogate model using two randomly selected strain histories of similar complexity. The figures also indicate the actual and predicted points of macroscopic first yield and damage initiation. In both cases, the surrogate model accurately predicts the strain–stress curves, the yielding and damage initiation, with an $E_{\sigma}$ of order 1–2 % for both random strain histories presented.

The surrogate model predicts the response to a typical random strain history in 30 s, using a workstation with 2 processors (Intel Xeon e5-2650 v4, 2.20 GHz) and 256 GB of RAM (this was used in all computations presented here). A corresponding FE prediction of the response to random strain histories requires approximately 3600 s of computation on the same hardware, providing computational savings of 2 orders of magnitude. We note that the VE examined here only comprises 1000 FEs. A typical RVE describing the response of a material element comprises many more elements, while the prediction time of the surrogate model is not affected by the size of the model used to produce the data; computational savings of several orders of magnitude are therefore possible by applying the proposed surrogate modelling technique.

To provide a benchmark for the predictions of the proposed surrogate model we compare them to those of a much simpler model, often used in the literature (we examined the accuracy of this simpler model for a heterogeneous elastic–plastic solid in [23]). The benchmark model performs the simple regression

$$\Delta\boldsymbol{\sigma} = NN(\boldsymbol{\varepsilon}, \boldsymbol{\sigma}, \Delta\boldsymbol{\varepsilon}) \tag{46}$$

The assumption in such benchmark model is that knowledge of the current strain and stress is sufficient to quantify all effects of previous history, including plastic deformation and development of damage. Fig. 14 presents the average and range of $E_{\sigma}$ for the two models, computed over 30 unseen random strain histories. The proposed data-driven model is approximately 10 times more accurate than the benchmark model in capturing the multi-axial response of the material. The stress versus strain predictions of the benchmark model lost agreement with the ground truth after the first few loading steps, while

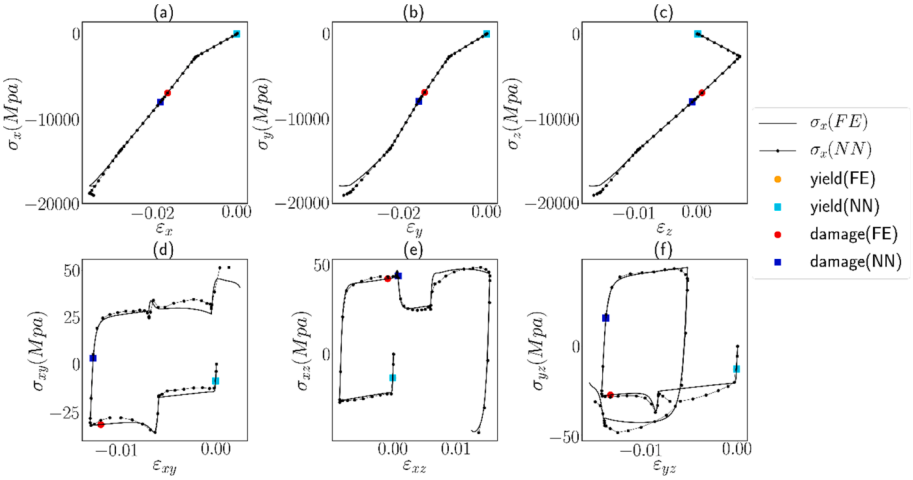



**Fig. 12.** An example of the performance of the surrogate model when predicting the stress history corresponding to a relatively simple strain history. $E_{\sigma} = 1.31\%$ in this case.

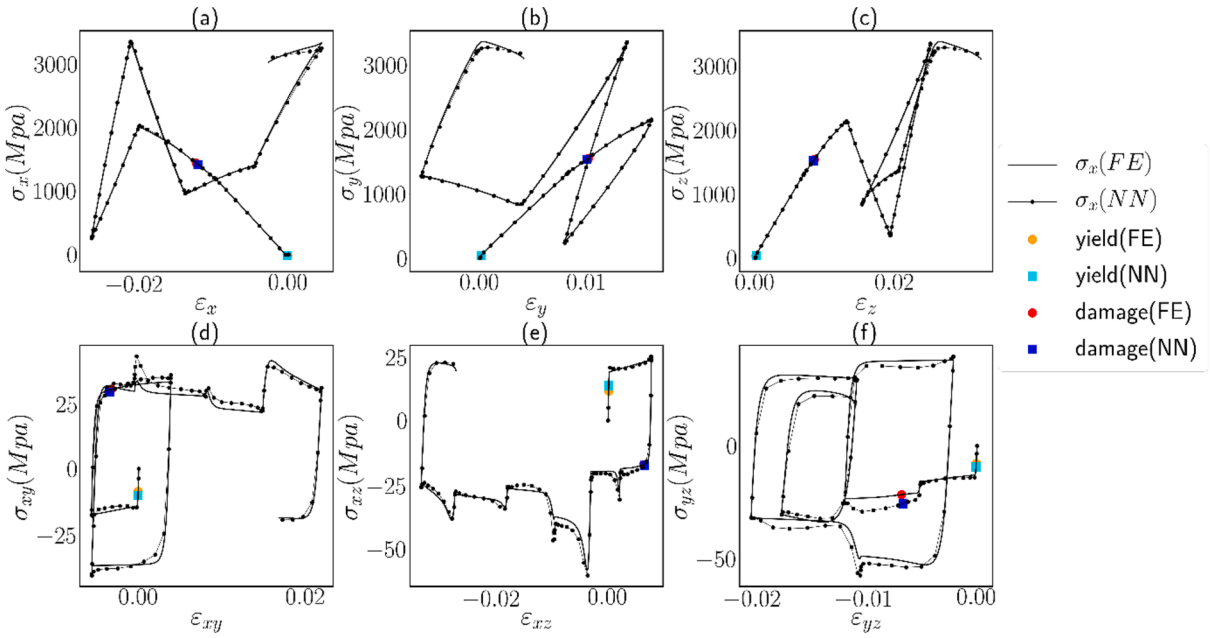



**Fig. 13.** Assessment of the accuracy of the surrogate model for a relatively complex imposed strain history. $E_\sigma = 1.17\%$ in this case.

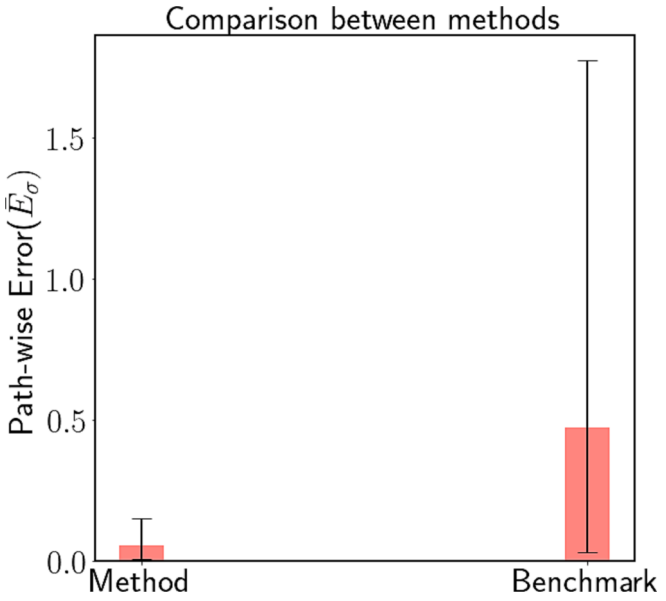



**Fig. 14.** A comparison between the proposed model and a benchmark model.

broadly retaining the correct trend. The comparison with the benchmark model highlights that it is important to include plasticity- and damage-related information as both inputs and outputs of the surrogate model.

## 5. Conclusions

We presented a computational framework to construct surrogate models of the response of elastic–plastic solids with progressive isotropic damage, subject to arbitrary strain histories. The surrogate model is trained on direct knowledge of the current material's stiffness matrix and it is able to compute the material response to imposed arbitrary histories of strain, including fully triaxial, non-proportional and non-monotonic loading, without the need for theoretical assumptions on the material's response. The data quantifying the progressive damage response of the material was produced by computing the evolution of the macroscopic stiffness matrix of the volume element, by repeated linear perturbation analyses. We assessed the accuracy of the surrogate model by predicting the stress history resulting from 30 random, unseen histories of applied strain, and found an average error of 5 % compared to the ground truth.

## 6. Declarations

### 6.1. Consent to participate

All authors of the manuscript are aware of and consent to the submission of this manuscript.

### 6.2. Availability of data and material

The raw data required to reproduce the findings of this study will be available in the near future from the corresponding author.

### 6.3. Code availability

The code for the surrogate model cannot be shared at present.

*CRediT authorship contribution statement*

**Weijian Ge:** Conceptualization, Methodology, Writing – original draft. **Vito L. Tagarielli:** Conceptualization, Supervision, Writing – review & editing.

## Declaration of competing interest

The authors declare that they have no known competing financial interests or personal relationships that could have appeared to influence the work reported in this paper.

## Data availability

Data will be made available on request.

## References


[1] S. Saeidi and J. L. Chaboche, 'Continuum Damage Mechanics: Part I-General Concepts', 1988, Accessed: Aug. 24, 2022. [Online]. Available: http://asme.org/terms.

[2] A. Sancho, et al., Experimental techniques for ductile damage characterisation, Procedia Struct. Integrity 2 (2016) 966–973, https://doi.org/10.1016/J.PROSTR.2016.06.124.

[3] N. Bonfoh, P. Lipinski, A. Carmasol, S. Tiem, Micromechanical modeling of ductile damage of polycrystalline materials with heterogeneous particles, Int. J. Plast 20 (1) (Jan. 2004) 85–106, https://doi.org/10.1016/S0749-6419(03)00017-2.

[4] M. Shakoor, J. Gao, Z. Liu, W.K. Liu, A data-driven multiscale theory for modeling damage and fracture of composite materials, Lect. Notes Comput. Sci. Eng. 129 (2019) 135–148, https://doi.org/10.1007/978-3-030-15119-5_8/COVER.

[5] S. Ghosh, J. Bai, D. Paquet, Homogenization-based continuum plasticity-damage model for ductile failure of materials containing heterogeneities, J. Mech. Phys. Solids 57 (7) (Jul. 2009) 1017–1044, https://doi.org/10.1016/J.JMPS.2009.04.002.

[6] T. Lesičar, J. Sorić, Z. Tonković, Ductile damage modelling of heterogeneous materials using a two-scale computational approach, Comput. Methods Appl. Mech. Eng. 355 (Oct. 2019) 113–134, https://doi.org/10.1016/J.CMA.2019.06.013.

[7] D. Montes De Oca Zapiain, E. Popova, F. Abdeljawad, J. W. Foulk Iii, S. R. Kalidindi, and H. Lim, 'Reduced-Order Microstructure-Sensitive Models for Damage Initiation in Two-Phase Composites', 2018, doi: 10.1007/s40192-018-0112-0.

[8] K. Dorhmi, L. Morin, K. Derrien, Z. Hadjem-Hamouche, J.P. Chevalier, A homogenization-based damage model for stiffness loss in ductile metal-matrix composites, J. Mech. Phys. Solids 137 (Apr. 2020), https://doi.org/10.1016/J.JMPS.2019.103812.

[9] F. Abbassi, T. Belhadj, S. Mistou, A. Z.-M. & Design, and undefined 2013, 'Parameter identification of a mechanical ductile damage using Artificial Neural Networks in sheet metal forming', Elsevier 45 (2012) 605–615, https://doi.org/10.1016/j.matdes.2012.09.032.

[10] S. Baltic, et al., Machine learning assisted calibration of a ductile fracture locus model, Mater. Des. 203 (Mar. 2021) 109604, https://doi.org/10.1016/J.MATDES.2021.109604.

[11] N. Zobeiry, J. Reiner, R. Vaziri, Theory-guided machine learning for damage characterization of composites, Compos. Struct. 246 (2020), https://doi.org/10.1016/j.compstruct.2020.112407.

[12] H. Yang, H. Qiu, Q. Xiang, S. Tang, X. Guo, Exploring elastoplastic constitutive law of microstructured materials through artificial neural network—A mechanistic-Based data-Driven approach, Journal of Applied Mechanics, Transactions ASME 87 (2020) 9, https://doi.org/10.1115/1.4047208.

[13] A. Schowtjak, et al., Prediction of ductile damage evolution based on experimental data using artificial neural networks, Int. J. Solids Struct. 257 (2022) 111950, https://doi.org/10.1016/j.ijsolstr.2022.111950.

[14] J. Gerlach, et al., Data-driven ductile damage model for damage-induced material degradation in forming, Manuf Lett 35 (Aug. 2023) 1097–1102, https://doi.org/10.1016/J.MFGLET.2023.08.092.

[15] D. Le Hien Nguyen, D. Thi Thanh Do, J. Lee, T. Rabczuk, H. Nguyen-Xuan, Forecasting damage mechanics by deep learning, Materials & Continua CMC 61 (3) (2019) 951–977, https://doi.org/10.32604/cmc.2019.08001.

[16] A. Fontes, F. Shadmehri, Data-driven failure prediction of Fiber-Reinforced Polymer composite materials, Eng. Appl. Artif. Intel. 120 (2023) 105834, https://doi.org/10.1016/j.engappai.2023.105834.

[17] Y. Song, A. Schiffer, and V. L. Tagarielli, 'The effects of heterogeneous mechanical properties on the response of a ductile material', *Scientific Reports 2021 11:1*, vol. 11, no. 1, pp. 1–17, Sep. 2021, doi: 10.1038/s41598-021-97495-x.

[18] M. Ostoja-Starzewski, Material spatial randomness: From statistical to representative volume element, Probab. Eng. Mech. 21 (2) (Apr. 2006) 112–132, https://doi.org/10.1016/J.PROBENGMECH.2005.07.007.

[19] A. Duval *et al.*, 'Abaqus/CAE 6.14 User's Manual', *Dassault Systémes Inc. Providence, RI, USA*, vol. IV, no. June, 2014.

[20] A. Schowtjak, et al., Prediction of ductile damage evolution based on experimental data using artificial neural networks, Int. J. Solids Struct. 257 (Dec. 2022) 111950, https://doi.org/10.1016/J.IJSOLSTR.2022.111950.

[21] W. Tian, L. Qi, X. Chao, J. Liang, M. Fu, Periodic boundary condition and its numerical implementation algorithm for the evaluation of effective mechanical properties of the composites with complicated micro-structures, Compos. B Eng. 162 (2019), https://doi.org/10.1016/j.compositesb.2018.10.053.

[22] E. Andreassen, C.S. Andreasen, How to determine composite material properties using numerical homogenization, Comput. Mater. Sci 83 (Feb. 2014) 488–495, https://doi.org/10.1016/J.COMMATSCI.2013.09.006.

[23] W. Ge and V. L. Tagarielli, 'A computational framework to establish data-driven constitutive models for time-or path-dependent heterogeneous solids', doi: 10.1038/s41598-021-94957-0.

[24] R.H.J. Peerlings, R. De Borst, W.A.M. Brekelmans, M.G.D. Geers, Localisation issues in local and nonlocal continuum approaches to fracture, European Journal of Mechanics, A/solids 21 (2) (Mar. 2002) 175–189, https://doi.org/10.1016/S0997-7538(02)01211-1.

[25] P. Ladevèze, O. Allix, J.F. Deü, D. Lévêque, A mesomodel for localisation and damage computation in laminates, Comput. Methods Appl. Mech. Eng. 183 (1–2) (2000) 105–122, https://doi.org/10.1016/S0045-7825(99)00214-5.

[26] D.H. Allen, Homogenization principles and their application to continuum damage mechanics, Compos. Sci. Technol. 61 (15) (Nov. 2001) 2223–2230, https://doi.org/10.1016/S0266-3538(01)00116-6.

[27] B.E. Hobbs, H.B. Mühlhaus, A. Ord, Instability, softening and localization of deformation, Geol. Soc. Spec. Publ. 54 (1990) 143–165, https://doi.org/10.1144/GSL.SP.1990.054.01.15.